AIAA JOURNAL
Vol. 45, No. 6, June 2007

Effect of a Laser Pulse on a Normal Shock

H. Yan* and D. Knight†
Rutgers University, Piscataway, New Jersey 08854-8058
and
R. Kandala‡ and G. Candler§
University of Minnesota, Minneapolis, Minnesota 55455

DOI: 10.2514/1.18283

A numerical study was conducted to understand the effect of a single laser pulse on a normal shock and shock boundary layer interaction. The goal is to examine the capability of a pulsed laser energy deposition to momentarily move a normal (terminal) shock upstream in a mixed-compression inlet so as to counteract the effect of a disturbance that would move the normal shock downstream. Two numerical models were used. The perfect gas model for energy pulse was developed at Rutgers University, and the commercial software GASPex was used as the flow solver. The real gas model was developed at the University of Minnesota. The research was conducted in two phases. First, the 3-D interaction of a laser pulse with an isolated normal shock at Mach 2 was examined using the perfect gas and real gas models. A detailed comparison of the computed flowfields indicates that the principal details of the interaction are accurately predicted by the perfect gas model. Second, the perfect gas model was used to simulate the 2-D interaction of a laser pulse with a normal shock including the effects of the interaction of the shock wave with a turbulent boundary layer. Three different dimensionless energy levels ($\epsilon = 1, 10,$ and 100) were considered. The interaction at $\epsilon = 100$ demonstrated a prominent upstream movement of the normal shock and a significant though temporary increase in the length of the separation region due to interaction of the compression wave (induced by the energy spot) with the separated boundary layer.

Nomenclature

c_p	=	specific heat at constant pressure
c_v	=	specific heat at constant volume
E_e	=	electron energy per unit volume
P_r	=	Prandtl number
p	=	static pressure of the gas
p_e	=	electron pressure
Q_r	=	radiation energy
Q_T	=	energy of laser pulse
q_{e_j}	=	conduction flux components of electron energy
R	=	gas constant
R_o	=	focal radius in perfect gas model
r	=	radius
r_o	=	radius
T	=	temperature
T_o	=	total temperature
u_i	=	mass-averaged velocity
$\boldsymbol{V}$	=	flow velocity vector
V_o	=	focal volume
v_{s_i}	=	species diffusive velocity
w_s	=	rate of production of species s
ϵ	=	dimensionless energy level
ϵ_Q	=	absorption coefficient
ρ	=	density
τ_{ij}	=	viscous stress components

Subscripts

s	=	a species
∞	=	ambient value

Received 18 June 2005; revision received 30 August 2006; accepted for publication 3 February 2007.

*Research Assistant Professor, Department of Mechanical and Aerospace Engineering, 98 Brett Road. Senior Member AIAA.

†Professor, Department of Mechanical and Aerospace Engineering, 98 Brett Road. Associate Fellow AIAA.

‡Graduate Student, Department of Aerospace Engineering and Mechanics, 110 Union Street SE. Student Member AIAA.

§Professor, Department of Aerospace Engineering and Mechanics, 110 Union Street SE. Associate Fellow AIAA.

Introduction

AT MACH 2.5 and above, a mixed-compression inlet (Fig. 1) provides greater aerodynamic efficiency than an external compression inlet [1]. In a mixed-compression inlet, supersonic flow is decelerated through a series of oblique shocks ending with a quasi-normal (terminal) shock downstream of the inlet throat. The total pressure loss is mostly due to the normal shock. To achieve high inlet performance, it is desirable to position the normal shock as close to the throat as possible to minimize total pressure loss. However, vehicles encounter different types of disturbances in flight, such as atmospheric turbulence and disturbances arising from the compressor face. Those disturbances might cause the normal shock to be momentarily displaced upstream of the throat, resulting in inlet unstart [2–5]. An unstart causes a loss of propulsive efficiency and can cause an asymmetric pressurization of the wing that would require large control surface forces to maintain aircraft control. On the other hand, those disturbances might cause the downstream movement of the normal shock. This increases the total pressure loss and might cause flow separation due to interaction between the stronger normal shock and boundary layer.

Various techniques to control the normal shock have been investigated including mass injection/removal at the wall, vortex generators, and passive venting [3,6–8]. However, those methods are not fast enough for high supersonic flows, where the required actuation time must be in the range of milliseconds.

In this paper we examine the capability of pulsed laser energy to control the motion of the terminal shock without adversely affecting the inlet total pressure recovery or shock boundary layer interaction. We focus on the use of pulsed laser energy to momentarily move a normal shock upstream, thereby counteracting the effect of an expansion wave originating downstream (e.g., at the compressor face) which would move the normal shock downstream [9].

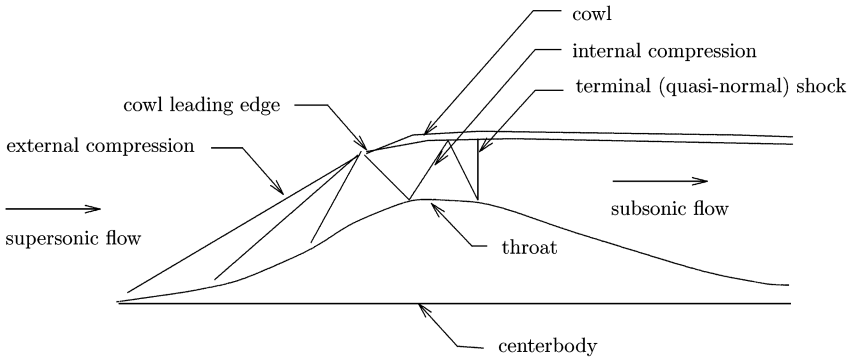

Fig. 1 Mixed-compression inlet.

The research is performed in two steps. First, the 3-D interaction of a laser pulse with an isolated normal shock at Mach 2 is examined using perfect gas and real gas models. The objective is to determine whether or not the perfect gas model provided an adequate description of the effect of the laser pulse on the shock motion. On the basis of detailed flowfield comparison, the perfect gas model is deemed acceptably accurate. Second, the perfect gas model is used to simulate the 2-D interaction of a laser pulse with a normal shock at Mach 1.5 including the effects of the interaction of the shock wave with a turbulent boundary layer.

Mathematical Models

Two separate models for laser energy deposition have been developed, namely, 1) a calorically and thermally perfect gas model, and 2) a real gas model. These two models were developed at Rutgers University and the University of Minnesota, respectively.

Perfect Gas Model

The inviscid perfect gas model assumes an initial Gaussian distribution for the static temperature in the spherical focal region of the laser pulse

$$T = T_\infty + \Delta T_o e^{-r^2/r_o^2} \tag{1}$$

where T_∞ is the temperature at the beginning of the energy deposition. The peak temperature rise ΔT_o is related to the total energy of the laser pulse Q_T by

$$\Delta T_o = \frac{\epsilon_Q Q_T}{\pi^{3/2} r_o^3 \rho_\infty c_v} \tag{2}$$

where r_o is chosen to be one-half of the radius R_o of the focal volume $V_o = \frac{4}{3}\pi R_o^3$, c_v is assumed constant, and ρ_∞ is the density at the beginning of the energy deposition. The coefficient ϵ_Q must be determined by comparison with experiment and is expected to be a function of the laser energy pulse Q_T and ambient conditions in the region of the energy deposition. The initial density in the focal region is assumed to be constant at the instant of energy deposition.

Despite its inherent simplicity, the model provides an accurate prediction of the flowfield outside of the focal volume and its immediate neighborhood. The model was validated by comparison with filtered Rayleigh scattering measurements [10]. The details are presented by Yan et al. [11].

The commercial computational fluid dynamics (CFD) software GASPex is used. The third-order accurate Roe scheme is used to compute the fluxes, along with the application of the min–mod limiter in each spatial direction to prevent numerical overshoots. The second-order Runge–Kutta scheme is used for the time integration. The k–ω turbulence model was used. GASPex automatically decomposes the entire domain into subdomains according to the memory resource of each processor and the number of CPUs.

Real Gas Model

The real gas model describes the laser energy deposition and subsequent flow evolution by the Navier–Stokes equations with extensions to include nonequilibrium thermochemisty and radiative transport. Air is modeled using 11 chemical species (N_2, O_2, NO, N, O, N_2^+, O_2^+, NO^+, N^+, O^+, and e). The governing equations are

$$\frac{\partial \rho_s}{\partial t} + \frac{\partial \rho_s u_j}{\partial x_j} = -\frac{\partial \rho_s v_{s_j}}{\partial x_j} + w_s \tag{3}$$

$$\frac{\partial \rho u_i}{\partial t} + \frac{\partial \rho u_i u_j}{\partial x_j} = -\frac{\partial p}{\partial x_i} + \frac{\partial \tau_{ij}}{\partial x_j} \tag{4}$$

$$\frac{\partial E_e}{\partial t} + \frac{\partial (E_e + p_e)(u_j + v_{s_j})}{\partial x_j} = -\frac{\partial q_{e_j}}{\partial x_j} - Q_{T-e} - Q_{e-v} + Q_r + w_e e_e \tag{5}$$

$$\frac{\partial E_v}{\partial t} + \frac{\partial E_v u_j}{\partial x_j} = -\frac{\partial q_{v_j}}{\partial x_j} - \frac{\partial}{\partial x_j}\sum_{s=1}^{n} v_{s_j} E_{v,s} + Q_{T-v} + Q_{e-v} + \sum_{s=1}^{n} w_s e_{v,s} \tag{6}$$

$$\frac{\partial E}{\partial t} + \frac{\partial (E + p)u_j}{\partial x_j} = -\frac{\partial}{\partial x_j}(q_j + q_{v_j} + q_{e_j}) + \frac{\partial u_i \tau_{ij}}{\partial x_j} - \frac{\partial}{\partial x_j}\sum_{s=1}^{n} v_{s_j} \rho_s h_s + Q_r \tag{7}$$

These equations represent the conservation of mass, momentum, electron energy, vibrational energy, and total energy, respectively. Additional details are presented by Kandala and Candler [12]. The

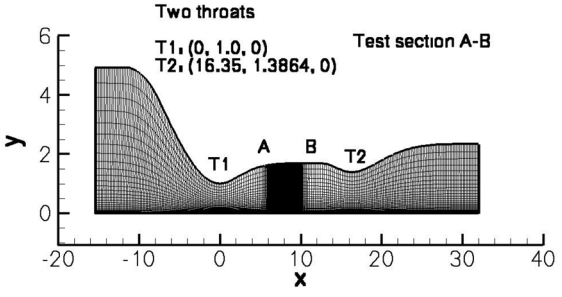

Fig. 2 Mach 2 supersonic tunnel.

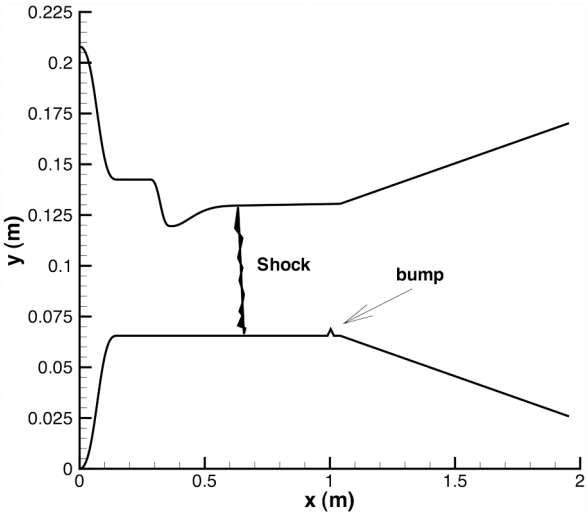

Fig. 3 Mach 1.5 supersonic tunnel.

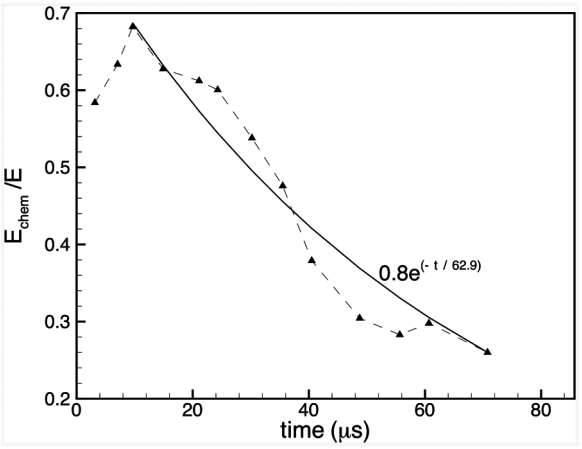

Fig. 4 Chemical relaxation time.

absorption and reflection parameters of the model were calibrated by comparison with the experimental data for shock radius vs time. Also note that the energy distribution in the focal volume is determined by the plasma formation model [12] and the energy spot is elongated along the laser incident direction, as observed in experiments.

A finite volume method is used with the third-order modified Steger–Warming flux vector splitting scheme. A monotone upstream-centered scheme for conservation laws (MUSCL) is used for variable reconstruction with a min–mod flux limiter. Time integration is the first-order accurate implicit Euler scheme.

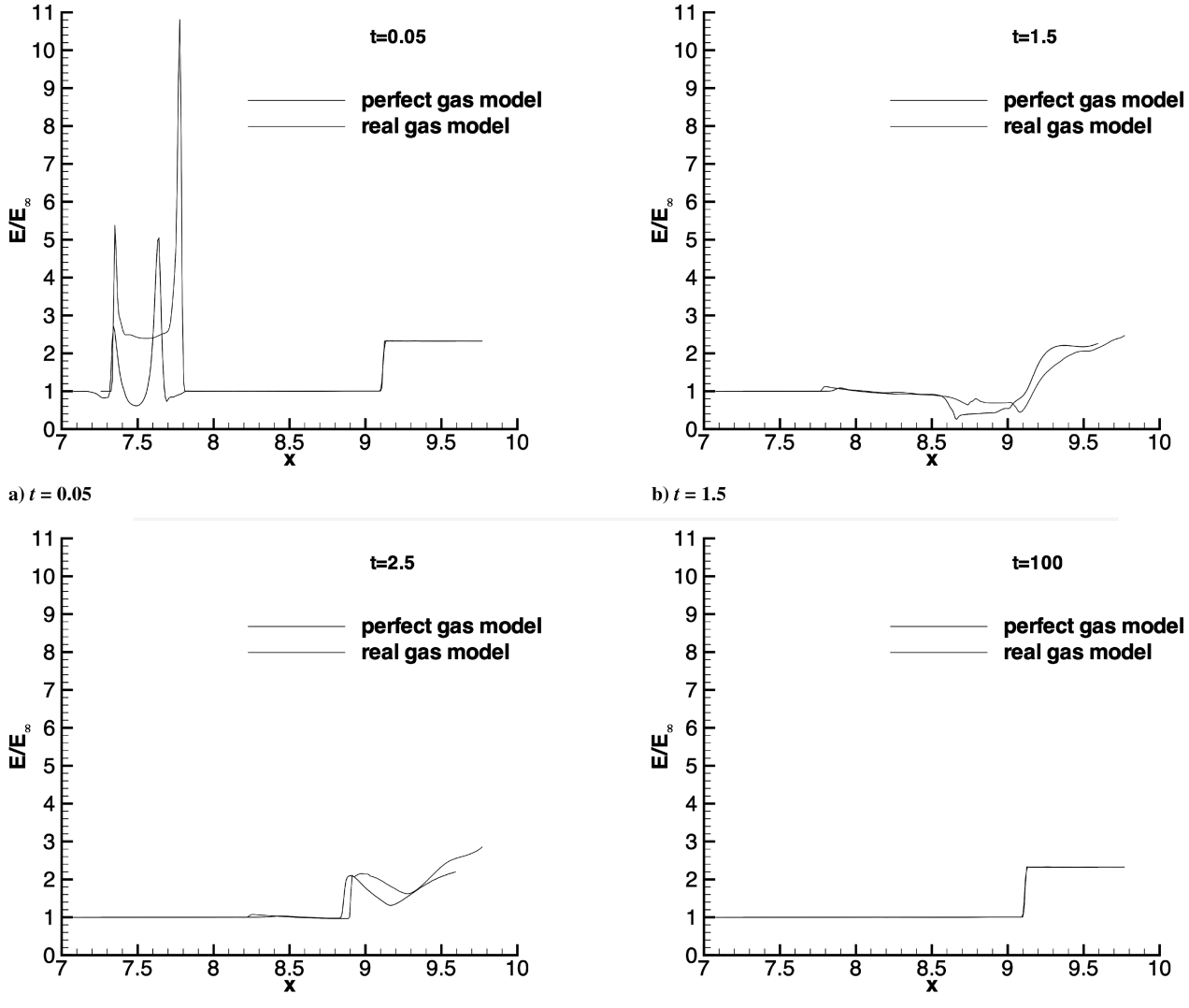

a) $t = 0.05$ b) $t = 1.5$

c) $t = 2.5$ d) $t = 100.0$

Fig. 5 Dimensionless total energy vs x for $\epsilon = 100$.

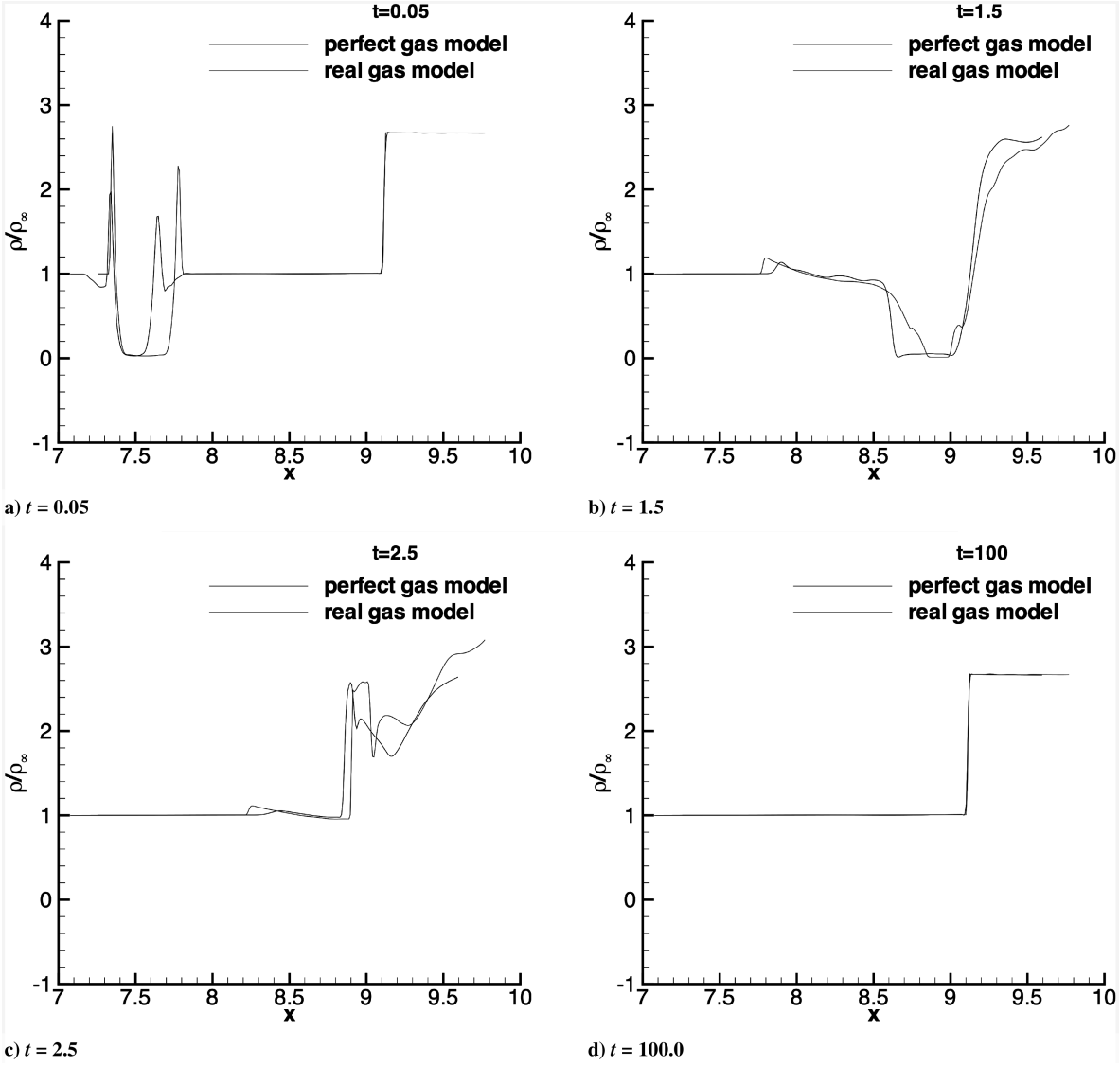

Fig. 6 Dimensionless density vs x for $\epsilon = 100$.

Flow Configurations

Two different flow configurations were considered. The first phase of the research examined the 3-D interaction of a laser pulse with an isolated normal shock at Mach 2 using both the perfect gas and real gas models. The second phase of the research examined the 2-D interaction of a laser pulse with a normal shock at Mach 1.5 including the effect of the shock wave turbulent boundary layer interaction using the perfect gas model.

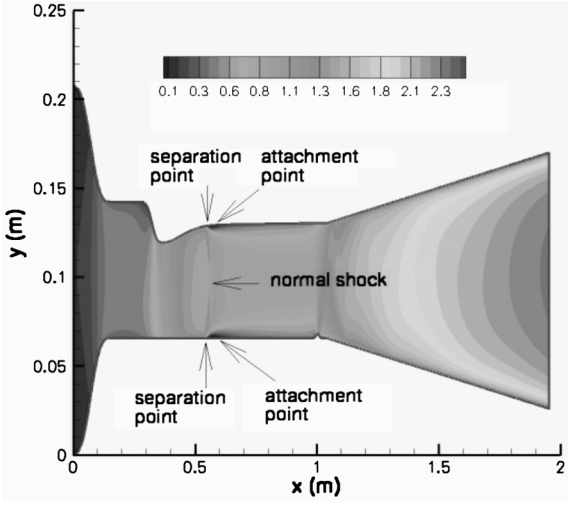

Fig. 7 Mach number contours.

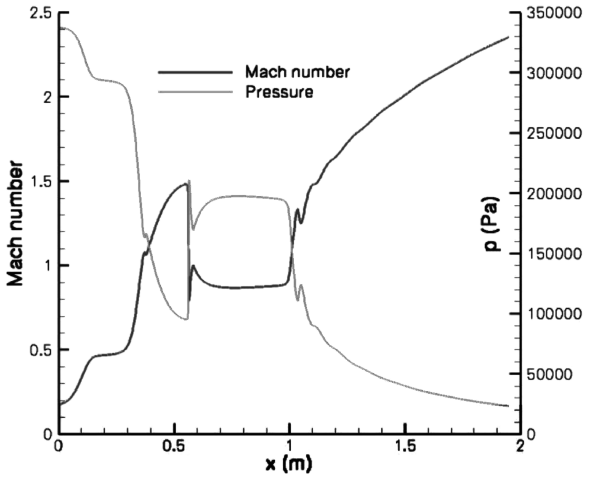

Fig. 8 Mach number and pressure along x before energy deposition.

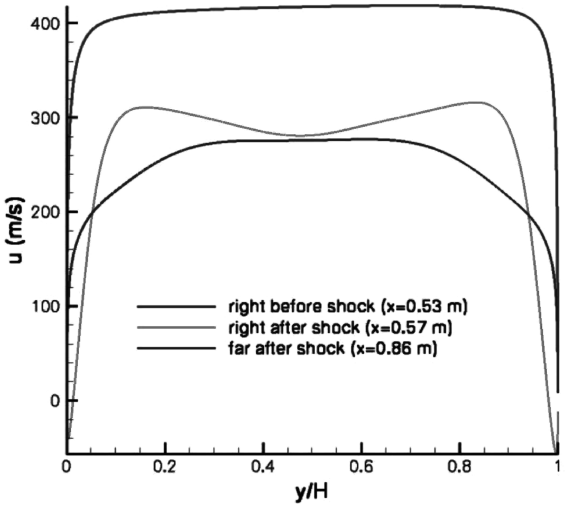

Fig. 9 Streamwise velocity at different locations before energy deposition.

Mach 2 Configuration

A normal shock is formed in a Mach 2 inviscid two-throat tunnel, which is designed following a classical inviscid design procedure proposed by Sivells [13] and shown in a dimensionless fashion in Fig. 2. The Mach 2 supersonic tunnel is composed of two throats, designated as $T1$ and $T2$. The test section A-B has a constant height. An incoming subsonic flow is accelerated to Mach 2 through the first throat, and a normal shock is formed in the section A-B. To eliminate the effect of disturbances propagating upstream to the shock location, the second throat is designed to accelerate the subsonic flow after the normal shock to a supersonic flow at the outflow boundary.

The half-height of the first throat is set to 1, and that of the second throat is 1.3864. The width is same as the half-height of the second throat. The entire three-dimensional computational domain is divided into three subdomains along the streamwise direction, among which the second one has the finest grid to capture the shock location and to resolve the initial energy spot. The $y = 0$ plane is the horizontal central plane, and the $z = 0$ plane is the vertical central plane.

Mach 1.5 Configuration

A terminal shock in a mixed-compression inlet is simplified as a normal shock formed in a Mach 1.5 viscous nozzle. Figure 3 shows the center plane of a Mach 1.5 wind tunnel, which was designed by a classical inviscid design procedure [13] and the Wilcox boundary layer code [14] was used to account for boundary layer effects with prespecified total pressure and temperature. The total pressure and total temperature are chosen to be 3.45×10^5 Pa and 288.9 K, respectively, which are in the range of experimental test values for a typical wind tunnel.

A subsonic flow enters a convergent–divergent nozzle and chokes at the throat. A normal shock is formed 0.2 m downstream of the

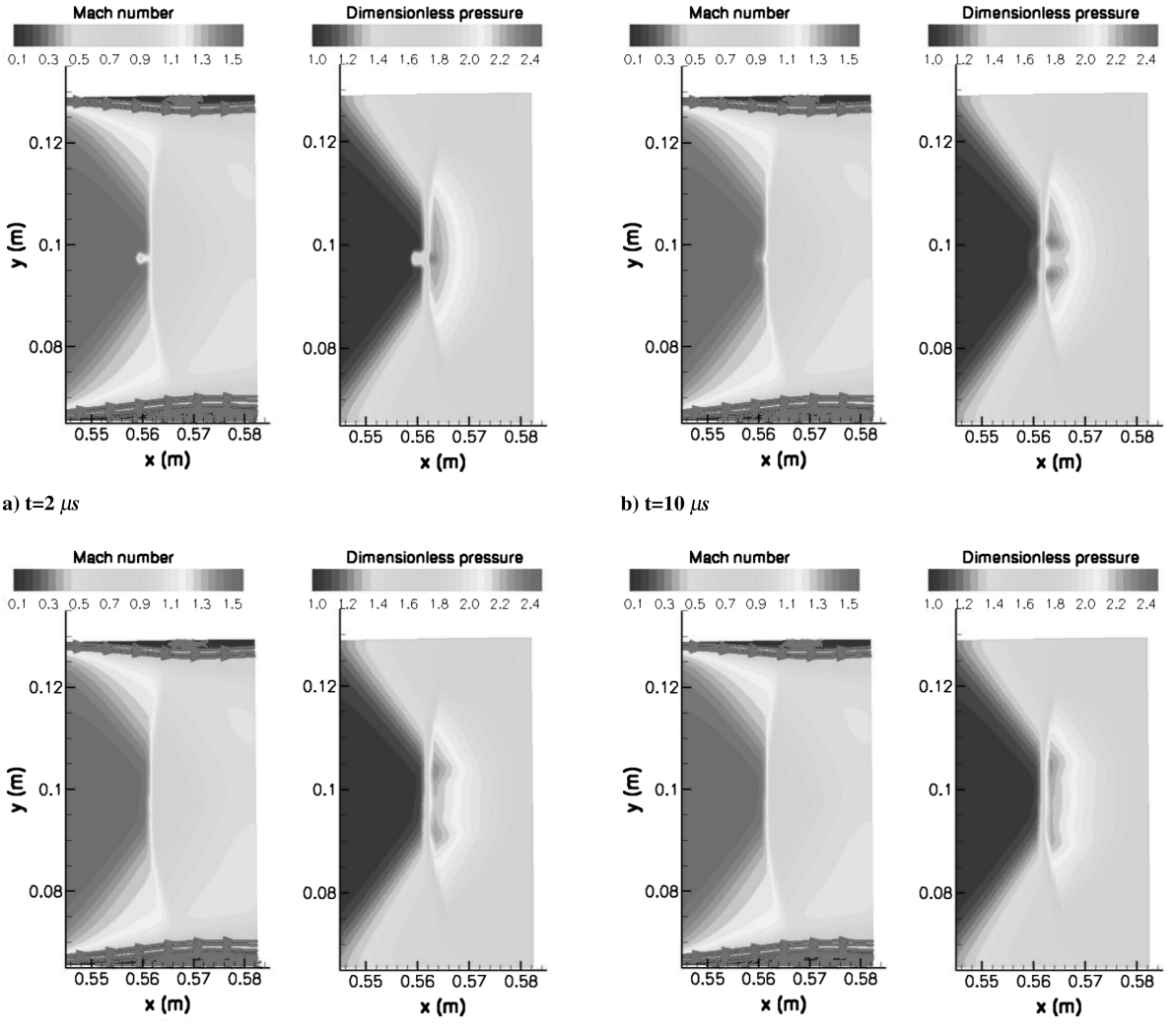

a) t=2 μs **b) t=10 μs**

c) t=20 μs **d) t=25 μs**

Fig. 10 Mach number, pressure contours, and streamlines at $\epsilon = 1$.

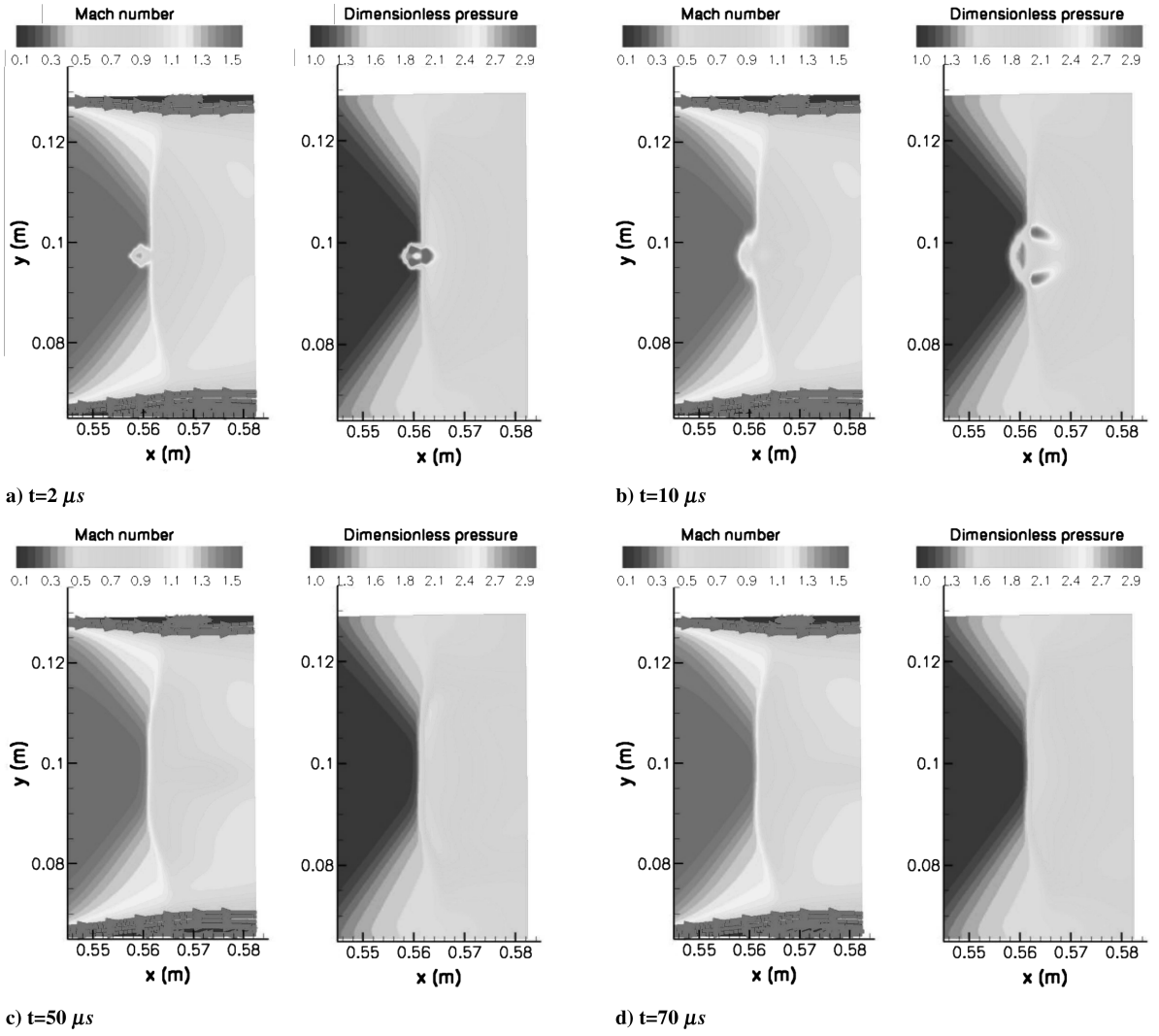

Fig. 11 Mach number, pressure contours, and streamlines at $\epsilon = 10$.

throat. To eliminate propagation of downstream disturbances that could adversely effect the stability of the normal shock, a small bump was added on the lower surface at the end of the test section to form a second throat which chokes the flow and accelerates the flow to supersonic at the exit.

Methodology

Three dimensionless parameters ($\epsilon, x_1/R_o, L/R_o$) are defined for the parametric study. The first parameter ϵ is used to measure the relative amount of energy deposited by the laser pulse and is defined as

$$\epsilon = \frac{\epsilon_Q Q_T}{\rho_\infty c_p V T_\infty} \tag{8}$$

The numerator $\epsilon_Q Q_T$ is the energy absorbed in the focal volume V. The denominator is the static enthalpy in region V at the beginning of the energy pulse. In the 2-D simulations, the energy spot is a circle and the numerator $\epsilon_Q Q_T$ is the energy per unit depth absorbed in the area V.

The second parameter x_1/R_o is used to measure the distance between the thermal spot and normal shock, where x_1 is the distance between the normal shock and the center of the laser focal volume and R_o is the radius of the energy spot assuming a spherical focal volume in the perfect gas model, or the maximum dimension of the laser spot in the real gas model. The third parameter L/R_o is used to measure the relative height of the normal shock to the hot spot radius, where L is the half-height of the tunnel at the shock location. For the three-dimensional inviscid Mach 2 flow, the value of L/R_o is set to be large enough to mimic the interaction of the laser pulse with a normal shock of infinite extent. For the two-dimensional viscous Mach 1.5 flow, the third parameter is not used.

The two numerical models were used for the simulation of the inviscid Mach 2 flow, and only the perfect gas model was used for the viscous Mach 1.5 flow. In the Mach 2 flow simulation, $\epsilon = 1$, 10, and 100 for both models. In the perfect gas model, $x_1/R_o = 20$ and $L/R_o = 20$, while in the real gas model, $x_1/R_o = 50$, 14, and 10 and $L/R_o = 50$, 14, and 10 for $\epsilon = 1$, 10, and 100, respectively. The value of L/R_o is large enough to mimic the interaction of the laser pulse with a normal shock of infinite extent. In the real gas simulations, the absorbed laser energy $\epsilon_Q Q_T$ is the fraction of the total deposited energy which is limited by the energy range of a Nd:YAG laser which is on the order of millijoules, and R_o is limited by the maximum dimension of the laser spot which is on the order of 5–10 mm. In dimensional terms, $R_o = 4.3$ mm.

In the Mach 1.5 flow simulation, the radius of the energy spot was taken to be the same as in the three-dimensional simulation, in which the focal volume was 3 mm^3 (consistent with experiment [1]) and was assumed to be spherical [11]. In this study, $x_1/R_o = 2.0$, and three energy levels were considered, $\epsilon = 1$, 10, and 100, which correspond to $Q_T = 0.83$, 8.3, and 83.0 J/m, respectively.

The grid is generated by the commercial software GridPro.[¶] The grid is refined in the test section to capture the normal shock and to resolve the laser spot. The normal shock location is captured within three grid cells. Twenty grid points are used to resolve the energy spot. The grid is stretched in the y direction with a stretch factor of

[¶]Data available online at www.gridpro.com [retrieved 20 January 2004].

1.01. The grid structure in the z direction is same as that in the y direction. For the viscous simulation, the grid resolution at the wall is $\Delta y^+ = 1.0$, which gives the minimum grid spacing of 0.00042 mm in the y direction and the grid is stretched in the y direction, and the grid spacing is 0.42 mm in the outer boundary layer. The total number of cells is 0.5×10^6 for the 3-D inviscid Mach 2 flow and 0.6×10^6 for the 2-D viscous Mach 1.5 flow.

For each simulation, the flowfield is first integrated in time until a steady state is reached with a normal shock formed. Thereafter, an energy pulse is added to the flow, and the flowfield is integrated in time.

Numerical Results

Normal Shock at Mach 2

The simulation starts without energy deposition to capture the normal shock. A supersonic flow is formed at the outflow boundary to eliminate downstream disturbances from propagating upstream to the normal shock. Once the steady normal shock is formed, a laser pulse is added at the $y = 0$ and $z = 0$ planes. Three simulations with a single laser pulse at different energy levels ($\epsilon = 1$, 10, and 100) deposited at the same location are performed using the two models.

The location of the normal shock in the test section is determined by the ratio of the first throat area to the second throat area in the perfect gas model. In addition, the static values at Mach 2 are important in the real gas model because the energy release due to chemical reaction and vibrational-electron energy transfer due to collisions between electrons and molecules is strongly dependent upon local flow static pressure and temperature. In the perfect gas model, the static values at Mach 2 are $T_\infty = 157$ K and $\rho_\infty = 0.667$ kg/m^3, while the real gas model solution converges to $T_\infty = 160$ K and $\rho_\infty = 0.71$ kg/m^3 at Mach 2. The predicted shock locations are $x = 9.1$ and $x = 9.6$ in the perfect gas and real gas models, respectively, where x is measured from the first throat

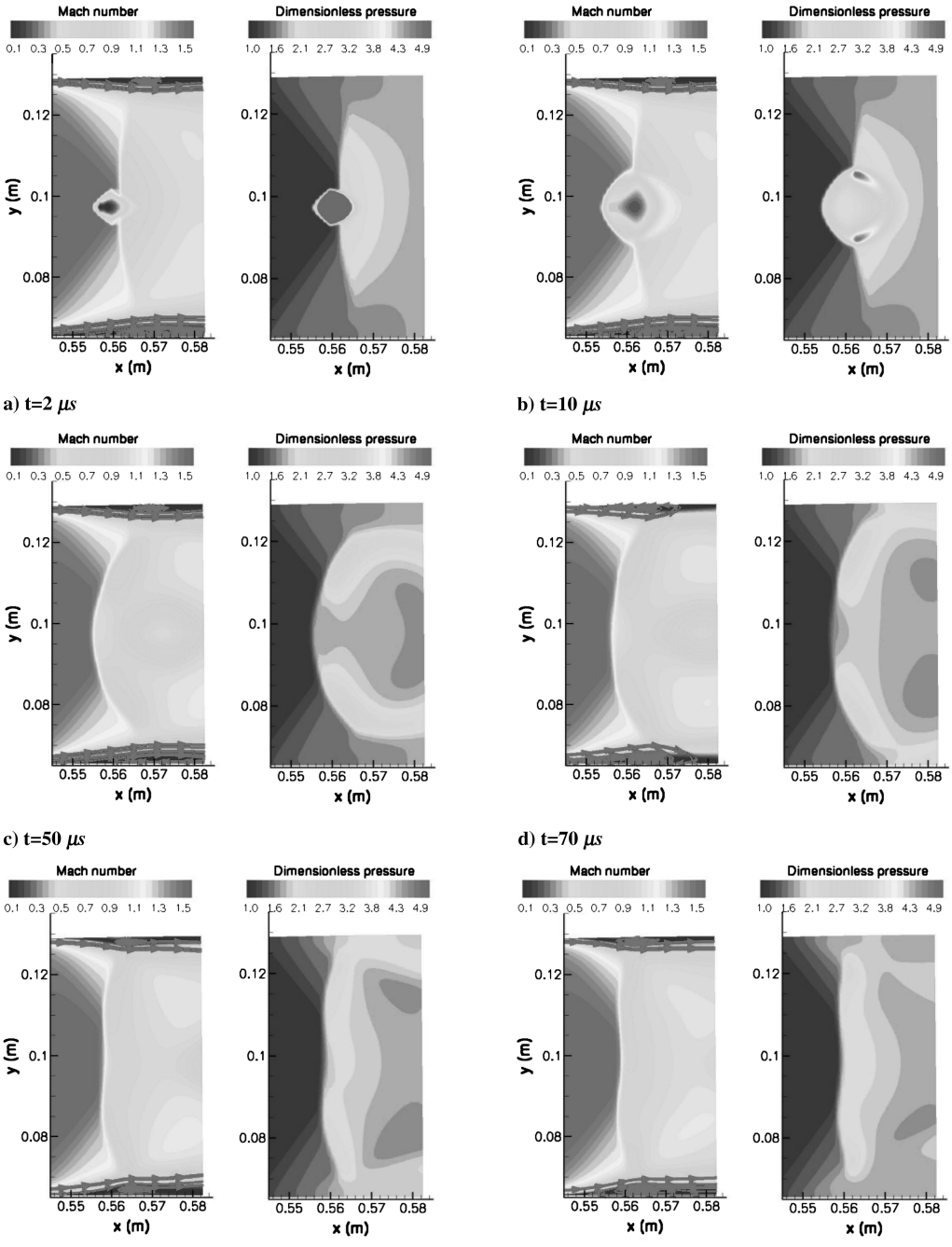

Fig. 12 Mach number, pressure contours, and streamlines at $\epsilon = 100$.

and nondimensionalized by the half-height of the first throat. The difference in the predicted shock locations is due to the slight difference in the static conditions upstream of the normal shock in the two models.

The laser pulse forms a high temperature and low density region with a blast wave propagating radially from the hot spot and an expansion wave propagating inward. The hot spot and its attendant waves convect downstream at the local velocity. In the real gas model, chemical reactions and ionization take place during the laser pulse, and then the gas begins to recombine, releasing the stored chemical energy to the flowfield. Figure 4 shows the change of the chemical energy with time, indicating that the chemical relaxation time is around 63 μs which is of the same order as the spot convective time of 85 μs, defined as x_1/u_∞, where u_∞ is the freestream velocity before the normal shock. This delayed chemical energy release affects the thermal spot evolution and is the main difference between the two models.

The normal shock is disturbed by the leading edge of the blast wave, the hot spot, and the trailing edge of the blast wave in sequence. The blast wave is observed to have little effect on the normal shock in both models because it weakens rapidly to essentially an acoustic wave before it reaches the shock. When the amount of the absorbed energy is the same as the local static enthalpy before the energy deposition ($\epsilon = 1$), the normal shock is essentially unaffected by the energy spot. However, with increased energy level, the upstream movement of the normal shock becomes more prominent due to the interaction of the shock with the hot spot which is characterized by a much lower Mach number. After all the disturbances move out of the postshock subsonic region, the normal shock returns to its original position. The hot spot is also distorted by its interaction with the normal shock, and its total energy per unit volume and density increase accordingly.

A quantitative comparison between the two models is shown in Figs. 5 and 6, which plot the total energy per unit volume and density variation along the symmetry line for $\epsilon = 100$. For the purpose of comparison, the heat of formation in the real gas model is excluded from the total energy per unit volume. The time t is a dimensionless variable defined as $t = t^*/(H/u_\infty)$, where t^* is dimensional time, H is the half-height of the first throat, and u_∞ is the velocity upstream of the normal shock. In the following figures, the predicted normal shock location in the real gas model is adjusted to match the perfect gas model to better compare the effect of the laser pulse and the interaction process between the two models. The two models predict the same total energy per unit volume and density difference cross the normal shock. They also predict similar total energy per unit volume and density variation for the energy spot and the interaction process. Shortly after the laser pulse, the total energy per unit volume and density increase dramatically across the blast wave, whereas the density decreases significantly toward the center of the spot due to the effect of the inward moving

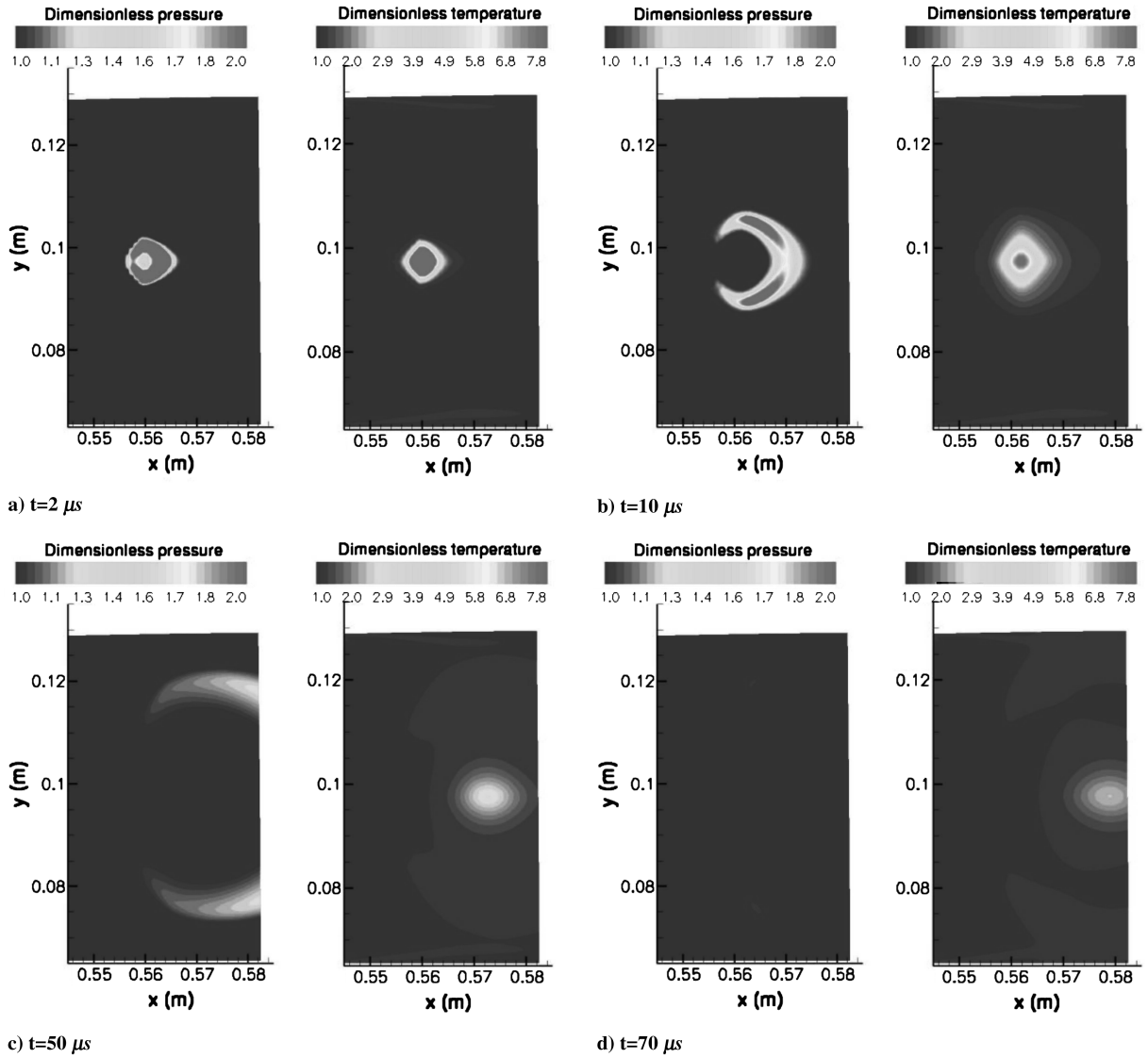

Fig. 13 Stagnation pressure and temperature contours at $\epsilon = 100$.

expansion fan. The two models predict the same level of the density reduction in the center of the spot.

However, the two models present some differences at the beginning of the energy deposition. First of all, the location of the blast wave is slightly different in the two models. This is due to the difference in the assumption of the shape of the focal volume in the two models. The focal volume is a sphere in the perfect gas model, while it is elongated in the laser incident direction (the assumed laser beam direction is from left to right in this computation) and has a narrow width in the radial direction in the real gas model. The total energy per unit volume in the perfect gas model is much higher than that in the real gas model as shown in Fig. 5a. This discrepancy is due to the assumption of initializing a spherical energy spot in the perfect gas model, which assumes that the energy is added instantaneously at constant volume (therefore the density is constant). The initially higher value of the pressure in the perfect gas model leads to a higher level of total energy per unit volume than in the real gas model. However, as the hot spot evolves, the pressure rapidly decreases due to the inward moving expansion wave. By the time that the hot spot reaches the normal shock, the distributions of total energy per unit volume in two models are similar as shown Fig. 5b.

In summary, the perfect gas and real gas simulations show similar results for the total energy per unit volume and density during the interaction of the hot spot with the normal shock. On the basis of this favorable comparison, the perfect gas model was used for the simulation of the interaction of a laser pulse with a Mach 1.5 normal shock including the shock wave turbulent boundary layer interaction.

Normal Shock at Mach 1.5

A Mach 1.5 normal shock is formed at $x = 0.2$ m downstream of the throat and separates the boundary layer as shown in Fig. 7. The Reynolds number based on the boundary layer thickness on the lower wall immediately before the shock is 3.3×10^5. A supersonic flow is formed at the outflow boundary to prevent downstream disturbances from propagating upstream to the normal shock. Figure 8 shows the Mach number and pressure distribution along x at $y = 0.9$ m, which crosses through the center of the focal volume for the energy spot. A small bump successfully chokes the flow at the end of the test section. The ratio of the cross section at the bump location to the throat is determined by a one-dimensional inviscid analysis with consideration of the boundary layer displacement effect.

According to Zheltovodov [15], turbulent boundary layer separation occurs in a normal shock wave boundary layer interaction when the Mach number exceeds approximately 1.2 (with a weak dependence on Reynolds number). Figure 9 shows the streamwise velocity profile along the y direction at three different streamwise locations. The streamwise velocity in the core region reaches a maximum right before the shock and decreases after the shock. The shock/boundary layer interaction causes boundary layer separation, leading to thickening of the boundary layer. The separation region on

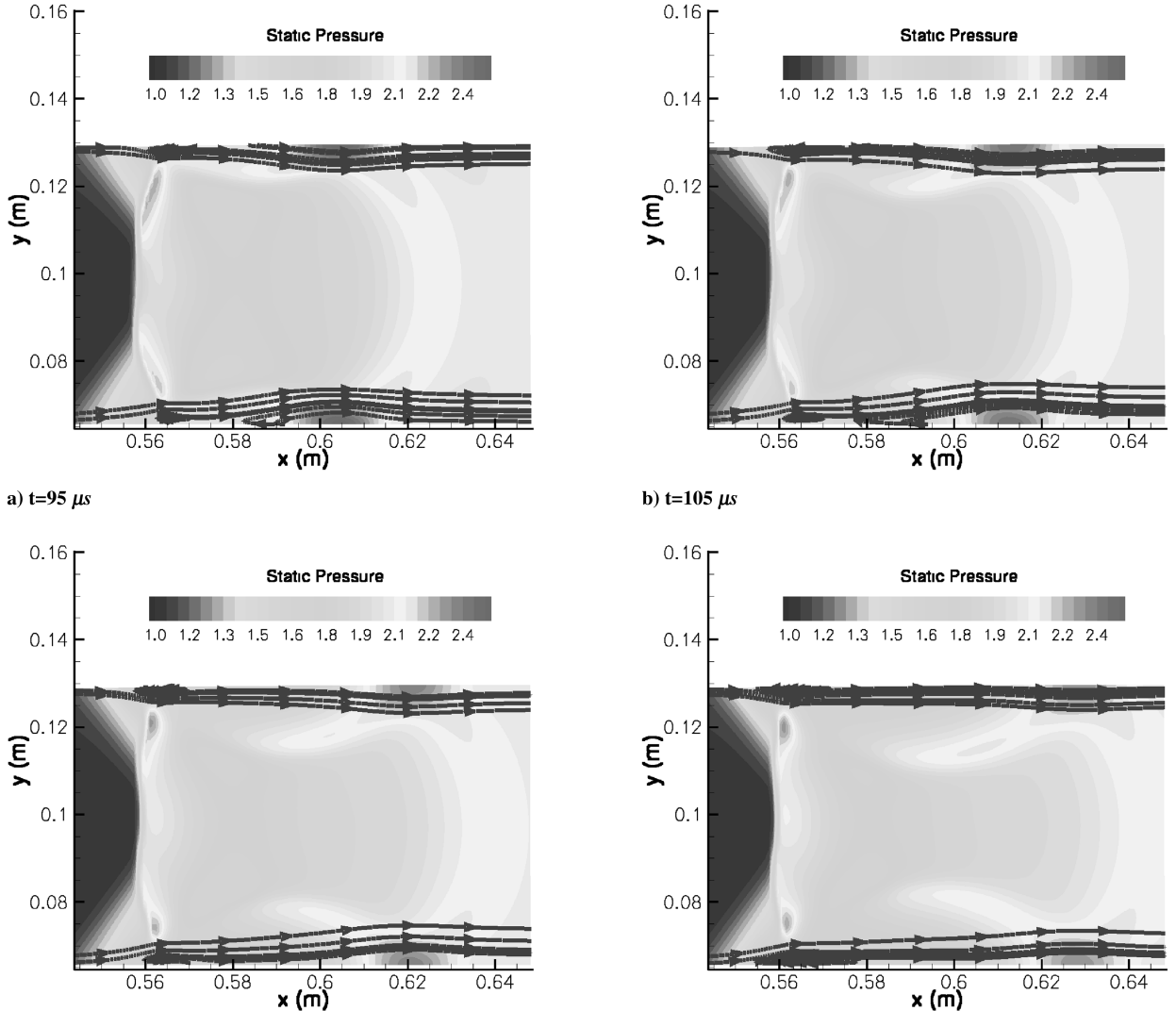

a) t=95 μs b) t=105 μs

c) t=115 μs d) t=125 μs

Fig. 14 Pressure contours and streamlines at $\epsilon = 100$.

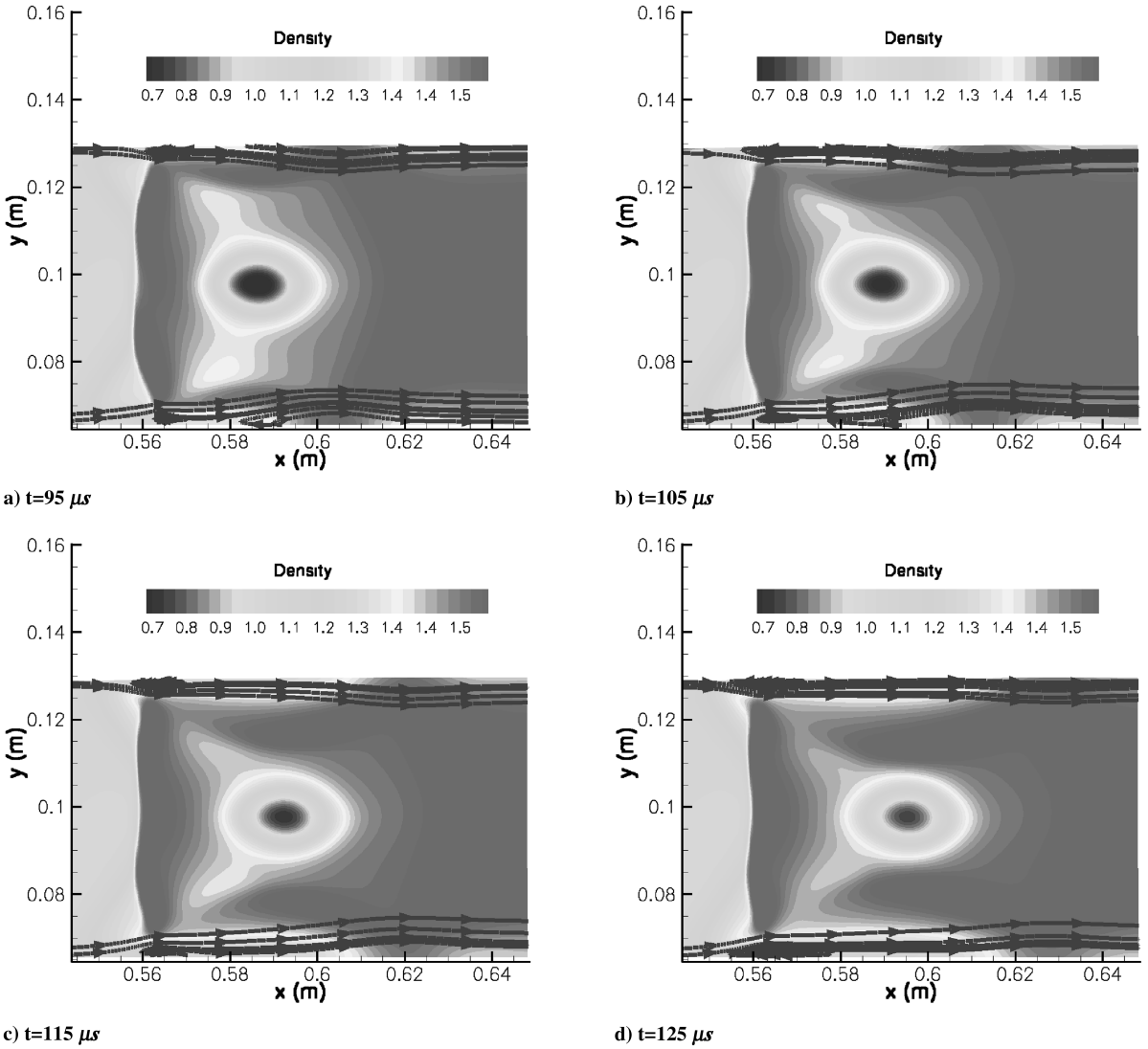

a) t=95 μs b) t=105 μs

c) t=115 μs d) t=125 μs

Fig. 15 Density contours and streamlines at $\epsilon = 100$.

the lower surface is 7.7δ long and 0.35δ high, and the one on the upper surface is smaller (4.8δ long and 0.23δ high) due to the curvature effect. The maximum reverse streamwise velocity is about 60 m/s, one-seventh of the maximum streamwise velocity right before the shock. The separation induced perturbation penetrates into the core region, causing distortion of the streamwise velocity. Far downstream of the shock, the core region flattens off, but the boundary layer grows thicker.

Once a stationary normal shock is captured, a circular energy spot is produced at a distance of $2R_o$ upstream of the shock in the middle of the cross section. A high temperature and low Mach number region forms with an instantaneously formed blast wave propagating from the hot spot and moving with the freestream toward the shock. Because the hot spot is very close to the shock, the blast wave front interacts with the shock in less than 1 μs, and it has negligible effect on the shock motion. Figures 10–12 represent a time sequence of the Mach number and pressure contours at $\epsilon = 1$, 10, and 100, respectively. The energy spot convects downstream, and its front quickly touches the shock around $t = 2$ μs at a relatively high speed (Figs. 10a, 11a, and 12a); then the movement of the energy spot is slowed down after it convects into the subsonic region. As the energy spot moves downstream, the resulting pressure waves expand into the surrounding flow, causing the local flow compression and expansion. The low Mach number region in the energy spot distorts the shock and pulls the shock upstream. Adelgren et al. [16] used a one-dimensional theory to explain this interaction between the shock and the energy spot. For $\epsilon = 100$, the maximum distance of the shock upstream movement is 1.7 times the radius of the initial energy spot.

The effect of a line energy source is quite different from that of a spherical energy pulse at the same ϵ value. Previous research [11,12] demonstrated that a spherical energy pulse had a relatively small region of influence. However, for a cylindrical line source perpendicularly incident to the flow, its region of influence is much wider than a spherical energy pulse [17]. As clearly seen in Figs. 12c and 12d, the region of influence starts to penetrate into the boundary layer. At the lower energy level ($\epsilon = 1$ and 10), the separation bubble hardly changes. However, at the higher energy level ($\epsilon = 100$), when the energy spot dissipates energy due to viscous effects, compression waves induced by the energy spot interact with the separation region, leading to a significant change in the flow structures. Figure 13 show a time series of the total pressure and total temperature contours at $\epsilon = 100$. The total pressure and temperature increase due to the energy pulse. With the energy for the energy spot dissipating into the surrounding flow, the total pressure and total temperature decrease, but they remain above the postshock values.

The flow structures in the separation region are shown in Figs. 14 and 15. The compression waves induced by the energy spot convect downstream and interact with the boundary layer, leading to the formation of a high pressure region downstream of the separation bubble. This high pressure region moves downstream and its location corresponds to the compression wave front as shown in Fig. 14. The change in the size of the separation region on the lower wall is shown in Fig. 16. The separation point remains essentially fixed, while the attachment point moves downstream, leading to a larger separation length on the wall. The separation region is stretched along the wall due to the interaction of the compression waves with the boundary

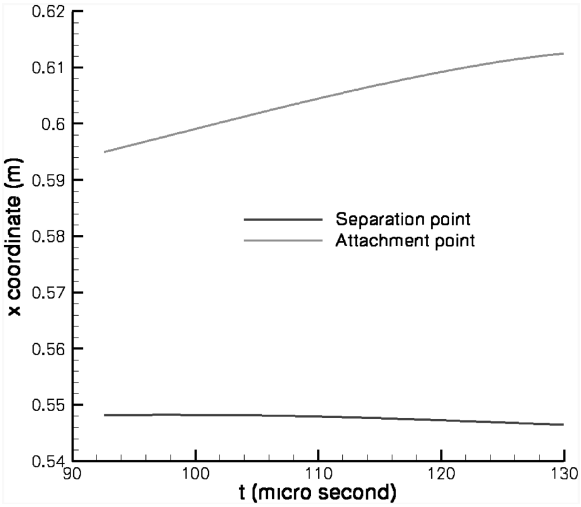

Fig. 16 Separation and attachment points.

layer and grows by 42% in the time period shown, before relaxing back to its original size.

Practical Impact

It is useful to estimate the energy required for significant movement of a normal shock at typical flight conditions for an airbreathing vehicle. Consider a vehicle at Mach 3 and an altitude of 10 km. Assume that the compression upstream of the terminal shock is nearly isentropic, and that the Mach number immediately upstream of the terminal shock is $M_s = 1.5$. For a laser spot with $R = 1$ mm, the energy corresponding to $\epsilon = 100$ is 387 mJ. This is a relatively low energy level and achievable with modern lasers. Of course, many practical engineering considerations need to be addressed. Also, the combination of laser plus microwave (using the laser to generate an initial region of sufficiently high electron density) may also prove effective.

Conclusions

Control of the location of the terminal shock in a mixed-compression inlet is a critical problem in modern aerodynamics. The dual objectives of terminal shock stability and high inlet total pressure recovery are in direct conflict with one another, i.e., positioning the terminal shock closer to the throat results in higher total pressure recovery but lower stability. Momentary movement of the terminal shock upstream of the throat due to disturbances emanating from the freestream or compressor may result in inlet unstart and subsequent dramatic reduction in total pressure recovery. Consequently, control of the location of the terminal shock is crucial to achieving high performance.

We examine the capability of pulsed laser energy to control the motion of a single normal shock as a model for the terminal shock in a mixed-compression inlet. In particular, we examine the capability of pulsed laser energy to force an upstream movement of the normal shock, as a model control mechanism for counteracting the downstream motion of a terminal shock due to a compression wave emanating from the freestream or expansion wave originating from the compressor face.

Two flow configurations were selected, and three laser pulse energy levels were considered. A 3-D Mach 2 inviscid simulation was performed to study the effect of a single energy pulse on a normal shock of infinite extent using perfect gas and real gas models. Results indicate that the primary effects of the energy pulse on the normal shock can be predicted using the perfect gas model. A 2-D Mach 1.5 perfect gas viscous numerical simulation was performed to study the effect of a single energy pulse on a normal shock and separation region resulting from the shock wave boundary layer interaction. Significant upstream movement of the shock was achieved for the highest energy level case. In the viscous case, the interaction of the energy spot with the shock causes a significant change in the flow structures, leading to an increase in the length of the separation region and the formation of a high pressure region downstream of the separation region. The high pressure region slowly moves downstream. The total pressure increases at the initial stages of the energy deposition and remains above the freestream value and the aftershock value, indicating that the energy deposition does not cause a decrease of the stagnation pressure. These results suggest that energy deposition by laser pulse has a significant potential for control of the motion of a terminal shock in a mixed-compression inlet.

Acknowledgments

This research is supported by the U.S. Air Force Office of Scientific Research (AFOSR) under Grant No. FA9550-04-1-0177 monitored by John Schmisseur. The 3-D computations were performed at Rutgers University and the University of Minnesota, and the 2-D computations were performed at Rutgers University and at the National Center for Supercomputing Applications (NCSA). The authors would like to thank Ramesh Balakrishnan for his assistance with the computations at NCSA.

References

[1] Kerrebrock, J., *Aircraft Engines and Gas Turbines*, 2nd ed., MIT Press, Cambridge, MA, 1992.
[2] Barry, F. W., "Frequency of Supersonic Inlet Unstarts Due to Atmosphere Turbulence," NASA CR-137482, Oct. 1972.
[3] Goldsmith, E., and Seddon, J., *Practical Intake Aerodynamic Design*, Blackwell Scientific Publications, Victoria, Australia, 1993.
[4] Kantrowitz, A., and Donaldson, C., "Preliminary Investigation of Supersonic Diffusers," NACA Rept. ACR No. L5D20, May 1945.
[5] Mayer, D., and Paynter, G., "Prediction of Supersonic Inlet Unstart Caused by Freestream Disturbances," AIAA Paper 1994-0580, Jan. 1994.
[6] Delery, J., and Marvin, J. D., "Shock-Wave Boundary Layer Interactions," AGARD Rept. AG-280, Feb. 1986.
[7] Hamed, A., and Shang, J. S., "Survey of Validation Data Base for Shockwave Boundary Layer Interactions in Supersonic Inlets," *Journal of Propulsion and Power*, Vol. 7, No. 4, 1991, pp. 617–625.
[8] McCormick, D. C., "Shock-Boundary Layer Interaction Control with Low-Profile Vortex Generators and Passive Cavity," *AIAA Journal*, Vol. 31, No. 1, 1993, pp. 91–96.
[9] Culick, F., and Rogers, T., "The Response of Normal Shocks in Diffusers," *AIAA Journal*, Vol. 21, No. 10, 1983, pp. 82–90.
[10] Boguszko, M., and Elliott, G., "On the Use of Filtered Rayleigh Scattering for Measurements in Compressible Flows and Thermal Fields," *Experiments in Fluids*, Vol. 38, No. 1, 2005, pp. 33–49.
[11] Yan, H., Adelgren, R., Boguszko, M., Elliott, G., and Knight, D., "Laser Energy Deposition in Quiescent Air," *AIAA Journal*, Vol. 41, No. 10, 2003, pp. 1988–1995.
[12] Kandala, R., and Candler, G., "Numerical Studies of Laser-Induced Energy Deposition for Supersonic Flow Control," *AIAA Journal*, Vol. 42, No. 11, 2004, pp. 2266–2275.
[13] Sivells, J., "Aerodynamic Design of Axisymmetric Hypersonic Wind Tunnel Nozzles," *Journal of Spacecraft and Rockets*, Vol. 7, No. 11, 1970, pp. 1292–1299.
[14] Wilcox, D. C., *Turbulence Modeling for CFD*, DCW Industries, Inc., La Canada, CA, 1993.
[15] Zheltovodov, A. A., "Shock Waves/Turbulent Boundary-Layer Interactions—Fundamental Studies and Applications," AIAA Paper 1996-1977, June 1996.
[16] Adelgren, R., Boguszko, M., and Elliott, G., "Experimental Summary Report—Shock Propagation Measurements for Nd:YAG Laser Induced Breakdown in Quiescent Air," Department of Mechanical and Aerospace Engineering, Rutgers University, Oct. 2001.
[17] Yan, H., Knight, D., Kandala, R., and Candler, G., "Control of Normal Shock by a Single Laser Pulse," AIAA Paper 2004-2126, June 2004.

H. Chelliah
Associate Editor